Featured in Physics

Tailoring hierarchical nanoporous gold on dual length scales

Lukas Riedel,[1] Jürgen Markmann,[1,2] Jörg Weissmüller,[2,1] and Shan Shi[3,1,*]

[1]*Institute of Materials Mechanics, Helmholtz-Zentrum Hereon, D-21502 Geesthacht, Germany*

[2]*Institute of Materials Physics and Technology, Hamburg University of Technology, D-21073 Hamburg, Germany*

[3]*Research Group of Integrated Metallic Nanomaterials Systems, Hamburg University of Technology, D-21073 Hamburg, Germany*

(Received 30 May 2023; accepted 2 October 2023; published 15 November 2023)

Dealloyed nanoporous metals with a hierarchical structure provide model systems for low-density structural and functional nanomaterials. It has been suggested that these materials are distinguished by particularly stringent design principles, with precisely defined characteristic length scales, and with geometrically similar structures on each hierarchy level, and that the length scales can be independently tuned on each level. Studying nanoporous gold made by two-step dealloying, we here demonstrate the tunability of the microstructure, independently for the upper and the lower hierarchy level. Small-angle (SAXS) and ultrasmall-angle x-ray scattering (USAXS) revealed sharp interference peaks corresponding to each of the two levels, confirming the stringent structural definition. Exploiting USAXS, we resolve and study upper-hierarchy-level ligament spacings of up to 600 nm. The length scales inferred from the peak positions correlate excellently with structure sizes determined by analysis of electron micrographs. This suggests a scaling factor that allows for size conversion between the two approaches. Furthermore, the analysis of the small-angle scattering enables a characterization of the volume-specific surface area, in good agreement with the estimate based on the ligament size and the leveled-wave model as an approximate description of the material's microstructure.

DOI: 10.1103/PhysRevMaterials.7.116001

I. INTRODUCTION

Hierarchical nanoporous metals made by dealloying [1–9] combine a large specific surface area for functionalization at the lower hierarchy level with large open pore channels for transport at the upper level [3,9–11], and this makes them attractive as advanced surface-controlled functional materials. Applications as actuators, sensors, energy storage devices, and catalysts are under consideration [12,13]. The range of densities accessible to dealloying is restricted by the severe loss of internal connectivity at reduced solid fraction [14]. Structural hierarchy has been demonstrated as a pathway for mitigation, affording enhanced mechanical properties at a given solid fraction [8] as well as exceptionally low solid fraction by dealloying [6,8,13]. This opens perspectives in the field of lightweight materials.

Nanoporous solids can be prepared with a hierarchy of multiple length scales [12,15–17]—particularly compelling, dealloying-made nested-network nanoporous materials with geometrically similar structures on two distinct length scales. This was first demonstrated in [3], and a recent refinement of the preparation protocol provides uniform, millimeter-sized monolithic bodies of hierarchical nanoporous gold (HNPG) [8]. It has been suggested that refining that protocol will afford the independent tuning of the microstructural characteristics, separately on each of the hierarchy levels [8]. Here, we present preparation and characterization of HNPG confirming the suggestion.

The central microstructural characteristics of a nanoporous metal are its ligament size and its solid fraction. Scanning electron microscopy (SEM) is applied routinely for characterizing size. Yet, investigating representative and statistically meaningful ensembles of microstructural features is typically a challenge with that approach. Furthermore, applying different analysis approaches to the same micrograph can yield significantly different results for the ligament size [18]. Hierarchy aggravates that issue, since it requires microstructural features to be characterized separately on multiple length scales. Small-angle x-ray or neutron scattering offers an alternative that typically provides data representative of much larger and statistically meaningful ensembles. Several studies have applied those techniques to conventional (single length scale) nanoporous metals [19–28].

Small-angle scattering studies of nanoporous gold invariably observe a pronounced interference peak, suggesting a high degree of structural definition with a single dominant wavelength. This is reproduced by the leveled-wave model for the material's microstructure. The model, originally derived for early-stage spinodal decomposition [29], is obtained by superimposing plane waves of identical wavelength but different wave vector orientation and random phase shifts and then binarizing by a level cut. It has been found to well reproduce mechanical and topological properties of nanoporous gold (NPG) [14,30] and of each of the hierarchy levels of HNPG [8].

While first studies have successfully applied small-angle x-ray scattering (SAXS) to nested-network nanoporous gold [4] with self-similar network microstructures on two distinct

*Corresponding author: shan.shi@tuhh.de

length scales and to multiscale porous microstructures generated during the degradation of NPG-based lithium-storage materials [26], the large ligament size of the upper hierarchy level of the ordered nested-network material presents a challenge for the resolution of the method. The use of small-angle scattering approaches for quantifying microstructural characteristics of HNPG remains to be demonstrated. Here, we show that a combination of in-house SAXS and ultrasmall-angle x-ray scattering (USAXS) affords the simultaneous characterization, consistent with SEM, of structural length scales on two hierarchy levels in HNPG. Furthermore, we show that solid fraction and specific surface area can also be quantified.

Various measures for the characteristic microstructural length scale in nanoporous metals are in use and a basis for comparison is not always available. Even in the analysis of small-angle scattering data, procedures are not consistent between different studies. Our comparative data set affords a discussion of the relative magnitude for NPG, with an emphasis on procedures for extracting length scales consistently from the small-angle scattering data or, more generally, from interference functions.

II. METHODS

A. Preparation

Our synthesis of nanoporous gold with two hierarchy levels refines the 3-step protocol by Shi *et al.* [8]. The nanoporous product evolves through three stages, an initial nanoporous Ag-Au in stage (i), a coarsened nanoporous silver-gold (NPSG) in stage (ii), and a final hierarchical nanoporous gold in stage (iii). Starting out from a dilute solution of Au in Ag as the master alloy, the first step generates stage (i) by dealloying, taking care to ensure a high fraction, $x_{\mathrm{res}}^{\mathrm{Ag}}$, of residual Ag. The second step coarsens that material to stage (ii) by annealing, and the third step implements another dealloying process, removing the residual Ag and generating nanoporosity inside the ligaments, resulting in stage (iii).

The master alloy, of composition $Ag_{90}Au_{10}$, was prepared by arc melting (MAM-1 Edmund Bühler) of Ag wires (99.99%, WIELAND Edelmetalle) and Au wires (99.99%, Sindlhauser Materials). For homogenization, the ingot was sealed in a quartz glass tube under a vacuum of about 10^{-1} mbar, annealed at 850 °C for 5 days, and quenched in water. The homogenized ingot was cold rolled and subsequently cut in $0.8 \times 0.6 \times 0.6$ mm^3 cuboids using a diamond wire saw (Well 3032-4).

Dealloying was conducted in a 3-electrode chemical cell filled with aqueous electrolyte at room temperature. A coiled silver wire was used as the counter electrode and a homemade pseudo-Ag/AgCl-electrode as the reference electrode. The reference potential was determined as 0.621 ± 0.001 V versus a standard hydrogen electrode (SHE; HydroFlex, Gaskatel) in 0.01 M H_2SO_4 and 0.513 ± 0.004 V versus SHE in 1 M $HClO_4$. Before every dealloying procedure, the potential of the reference electrode was measured against a SHE to ensure its performance. All potential values stated in this work relate to the potential of the working electrode relative to the pseudo-Ag/AgCl-electrode. As potentiostat, a Metrohm Autolab PGSTAT302N was used.

The 1st dealloying was conducted in 0.01 M H_2SO_4 (98% Rotipuran). A dealloying potential $E_{\mathrm{D}} = 0.396$ V was applied until the charge density, defined as the charge transfer per mass, reached 517 C/g. This value, which is determined empirically, is required to obtain a composition of $Ag_{75}Au_{25}$ in the dealloyed sample. After dealloying, the samples were cleaned in ultrapure water (Sartorius Arium Comfort, conductivity 0.055 μS/cm) for 6–12 h and then in ethanol for 3–6 h.

To estimate the composition, the mass loss of every sample was measured after the 1st dealloying. Only samples with $0.73 \leqslant x_{\mathrm{res}}^{\mathrm{Ag}} \leqslant 0.77$ were selected for further synthesis steps. The accuracy of the mass measurement was assured by the comparison to energy-dispersive x-ray spectroscopy (EDS) on the fracture surface of an exemplary sample with $x_{\mathrm{res}}^{\mathrm{Ag}} = 0.75$ according to mass loss. A sequence of 12 measurements with EDS yielded $0.74 \leqslant x_{\mathrm{res}}^{\mathrm{Ag}} \leqslant 0.79$ with an average of $x_{\mathrm{res}}^{\mathrm{Ag}} = 0.77$.

Annealing as the 2nd step of the synthesis was performed in an infrared furnace (MILA-5000, ULVAC) at a vacuum of 5×10^{-6} mbar. Temperatures were $T_{\mathrm{A}} = 300$ °C, 400 °C, or 500 °C with a duration of 20 min.

The 2nd dealloying of the coarsened samples was conducted in 1 M $HClO_4$ (60% Emsure ACS, Merck Millipore) and consisted of 3 substeps. First, $E_{\mathrm{D}} = 0.76$ V, 0.80 V, or 0.83 V was applied for 2 hours. Second, a potential of 0.99 V was applied for 2 hours. Finally, 5 potential cycles within a range of 0.30 V and 0.95 V at a rate of 5 mV/s were applied. The counter electrode, silver wire, was replaced by a rolled piece of carbon cloth (Kynol activated carbon fabrics, specific surface area >1800 m^2/g) in the final substep. A cleaning procedure similar to the one after the 1st dealloying followed.

B. Microscopy and focused-ion-beam cutting

An optical microscope (Olympus SZX10), equipped with a calibrated reticle, was used to measure sample dimensions. In various stages of the preparation, solid fractions were determined from the mass and the volume as determined from the dimensions and the composition data.

On fracture surfaces of scalpel-cleaved nanoporous samples, high-resolution SEM images were acquired by a FEI Helios Nanolab G3. For composition analysis energy-dispersive x-ray spectroscopy (Oxford Instruments X-Max 80) was used. The average ligament diameter, L_{SEM}, was determined by measuring, using the software ImageJ [31], the diameter at the narrowest section of at least 25 ligaments. ImageJ's option "Analyze - Measure" was used for the operator to draw lines and to analyze their length. Figure S1 in the Supplemental Material [32] shows an exemplary micrograph with the diameters of the evaluation marked.

In preparation for the SAXS measurement, slabs with areas of about 0.5×0.5 mm^2 were cut with a plasma focused ion beam instrument (FEI Helios G4 PFIB). Their thicknesses emerged between 9 and 49 μm. Figure 1 shows an exemplary micrograph. The slabs were removed with a scalpel and transferred to scotch tape for mounting in the SAXS stage. The uniform and known thickness of the wall allows a quantitative analysis and a stronger scattering signal compared with powder-type SAXS samples.

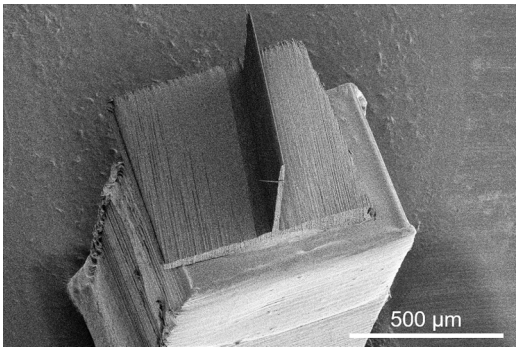

FIG. 1. Scanning electron micrograph of a focused-ion-beam-cut nanoporous gold sample for small-angle scattering. The center of the vertical slice is probed in the scattering experiment.

C. Small-angle x-ray scattering

Small-angle x-ray scattering used a point focus instrument (Xeuss 3.0) with a copper microfocus source (Genix 3D), a fully evacuated beam path, and a 2D solid-state detector (Pilatus 300K). For every sample, two measurements were conducted at sample-to-detector distances of 500 mm and 1800 mm. The beam full width at half maximum was 0.2 mm. For USAXS measurements, a Bonse-Hart module [33], using channel-cut monochromator and analyzer crystals, was entered into the beam path. SAXS data can be evaluated down to q values of 0.015 nm^{-1}, whereas USAXS explored the range between 0.1 nm^{-1} and 0.003 nm^{-1}. Here, q denotes the wave number, $q = 4\pi \sin(\theta)/\lambda$ with θ half the scattering angle and λ the wavelength.

The data reduction was based on the software XSACT by Xenocs [34]. All data were corrected for transmission and for background, that is, slit and substrate scattering. Transmission was determined by comparing intensity values at $q = 0$. Apart from the transmission correction, the intensity was referred to incident flux and sample thickness, yielding the differential scattering cross section, $d\Sigma/d\Omega$. The procedure was verified by application to a standard (glassy carbon) of known differential scattering cross section. As the SAXS data were radially isotropic on the detector, radial averaging was applied to all SAXS data sets.

For USAXS, part of the beam bypassed the sample, and this prevented data reduction to absolute units. The data reduction (using the USAXSGUI tool by Xenocs) applied background subtraction, desmeared [35] the data, and then scaled it to absolute units by splicing with the SAXS signal between $q = 0.06$ nm^{-1} and $q = 0.1$ nm^{-1}.

D. Analysis of scattering data

Similar to earlier small-angle scattering studies of NPG [4,20–22,24,27], we have evaluated the wave numbers, q_0, of the small-angle scattering interference peaks for determining the characteristic spacing, $\tilde{L}$, between neighboring ligaments. $\tilde{L}$ has also been reported as a metric defining the scale in modeling [14] or as an experimental size metric, based on Fourier transforms of electron micrographs [28,36,37].

To determine the q_0, the signal in logarithmic scaling was fitted by the sum of a Gaussian centered at q_0 and the baseline function $A[1 + (Bq)^C]^{-D}$ with adjustable parameters A, B, C, and D. Limits of the background function are A for $q \to 0$ and a $\propto q^{-CD}$ power law for $q \gg B^{-1}$. Scattering graphs featuring two peaks were fitted with two Gaussians and two baseline functions.

The relation between q_0 and $\tilde{L}$ [38],

$$\tilde{L} \approx 1.23\frac{2\pi}{q_0}, \tag{1}$$

derives from the position of the first maximum in the Debye scattering equation [39] for sets of randomly oriented pairs of scatterers (as, for instance, in a molecular gas) with a characteristic spacing $\tilde{L}$. Equation (1) also applies to the leveled-wave model as an approximation to the nanoporous-gold microstructure [14].

We note that the relation between the ligament spacing and the interference peak position is not consistently handled in the literature. Several studies [20,21,28,36,37] use $L = 2\pi/q_0$, ignoring the factor 1.23 in Eq. (1). While this provides a valid metric for a characteristic structural length scale, that metric does not represent the mean distance between ligaments. That distance emerges from the first maximum in the autocorrelation function and, as mentioned above, it is correctly related to the interference peak position by Eq. (1).

A measure of the total scattering intensity of a system is the invariant, Q, which may be obtained by integration of the radially averaged differential scattering cross section, $d\Sigma/d\Omega$, according to [40]

$$Q_S = \int_0^\infty \frac{d\Sigma}{d\Omega} q^2 dq. \tag{2}$$

For microstructures with two uniform phases, the invariant depends only on the difference in electron density between the phases. Specifically, for porous materials and x-ray scattering, one has [40,41]

$$Q_\varphi = 2\pi^2 \langle Z \rangle^2 r_e^2 \rho_0^2 \varphi(1-\varphi). \tag{3}$$

The symbols φ, r_e, and Z represent, respectively, the solid (volume) fraction, the electron radius, and the atomic number. The bracket denotes compositional averaging, taking the solid phase as a uniform solid solution of Au and Ag on the crystal lattice with site density ρ_0. When evaluating the integral of Eq. (2) for the experimental signal, we extrapolated $d\Sigma/d\Omega$ as a constant for $q \to 0$ and as $\propto q^{-4}$ for $q \to \infty$.

The scattering data afford estimates of the specific surface area, α (area per total volume). One approach is based upon Porod's law [40],

$$\alpha = \frac{\pi\varphi(1-\varphi)}{Q_S} \lim_{q\to\infty} \frac{d\Sigma}{d\Omega} q^4. \tag{4}$$

Note that conceivable errors in the reduction of the scattering data to absolute units cancel out because of the normalization to the invariant.

Another approach to α exploits its correlation with the dominant scattering vector q_0 through the function [14]

$$\hat{\alpha}(q_0, \varphi) = \frac{2q_0}{\pi\sqrt{3}} \exp\{-[\mathrm{erf}^{-1}(2\varphi - 1)]^2\}. \tag{5}$$

This approach is based on approximating the structure of NPG with the leveled-wave model.

TABLE I. Overview of preparation parameters and microstructural characteristics for stage (ii) nanoporous silver-gold (NPSG) and stage (iii) hierarchical nanoporous gold (HPNG) samples. Annealing temperature T_A, dealloying potential E_D, net solid fraction φ, electron-micrograph-derived ligament diameters L^{L}_{SEM} and L^{U}_{SEM}, as well as ligament spacings $\tilde{L}^{L}$ and $\tilde{L}^{U}$ on lower and upper hierarchy levels, respectively. Residual silver content x^{res}_{Ag} as measured with energy-dispersive x-ray spectroscopy (EDS). If both small- (SAXS) and ultrasmall-angle scattering (USAXS) data for the $\tilde{L}$ exist, then the average $\tilde{L}$ from both approaches is specified. Except for the two variations where HNPG, annealed at 400 °C, was dealloyed at 0.80 V or 0.83 V, the SEM image was taken on the same sample on which the SAXS/USAXS measurement was performed. While the ligament diameter refers to the samples whose structures are illustrated in Figs. 3 and 4, the solid fraction represents the mean value of 3–4 samples. For HNPG, the residual silver content is the mean value of 1–2 samples with EDS measurements at 3–5 different positions on each sample. In contrast, for NPSG x^{res}_{Ag} is determined by the mass measurement of 4–5 samples. All error bars in this table refer to the standard deviation.

Sample Type	T_A (°C)	E_D (V)	L^{L}_{SEM} (nm)	$\tilde{L}^{L}$ (nm)	L^{U}_{SEM} (nm)	$\tilde{L}^{U}$ (nm)	φ	x^{res}_{Ag}
NPSG	300				57 ± 10	162	0.40 ± 0.01	0.75 ± 0.01
	400				132 ± 31	291	0.42 ± 0.02	0.75 ± 0.01
	500				239 ± 56	637	0.44 ± 0.02	0.75 ± 0.00
HNPG	300	0.80	19 ± 3	59	59 ± 11	161	0.14 ± 0.00	0.06 ± 0.01
	400	0.80	19 ± 3	59	123 ± 25	287	0.15 ± 0.00	0.04 ± 0.01
	500	0.80	21 ± 3	64	201 ± 35	536	0.16 ± 0.01	0.04 ± 0.00
	400	0.76	29 ± 5	107	125 ± 17	321	0.13 ± 0.00	0.02 ± 0.00
	400	0.83	20 ± 3	46	115 ± 26	286	0.17 ± 0.00	0.05 ± 0.01

For the hierarchical material, two components contribute to the net specific surface area. The first component relates to the surface at the lower hierarchy level; its area is that of an extended network solid with the lower-hierarchy-level structure (solid fraction and wave numbers φ^{L} and q^{L}_{0}, respectively), but which only occupies that fraction of space which is given by the upper hierarchy level solid fraction, φ^{U}. The second component represents the surface at the upper hierarchy level. Its area is that of an extended network solid with the upper-hierarchy-level structure (solid fraction and wave numbers φ^{U} and q^{U}_{0}, respectively), yet only that fraction (namely φ^{L}) of its surface which intersects the network of the lower hierarchy level is actually present. Within the leveled-wave approximation, the net surface area of the hierarchical solid, per total volume, is therefore

$$\alpha^{H} = \varphi^{U}\hat{\alpha}\left(q^{L}_{0}, \varphi^{L}\right) + \varphi^{L}\hat{\alpha}\left(q^{U}_{0}, \varphi^{U}\right). \tag{6}$$

III. RESULTS AND DISCUSSION

We have investigated a series of samples, all based on the master alloy $Ag_{90}Au_{10}$, with an eye on tuning the upper hierarchy level ligament size, L^{U}, through varying the annealing temperature T_A and on tuning the lower-level ligament size, L^{L}, through variation of the dealloying potential E_D during the second dealloying. The results of the microstructure characterization—as presented below—are compiled in Table I.

A. Macroscale structure

Figure 2 shows an overview over the macroscopic geometry of our samples in various stages of preparation, passing from nanoporous Ag-Au after the first dealloying [stage (i), Fig. 2(a)] to the coarsened NPSG state after annealing [stage (ii), Fig. 2(b)] and finally to the hierarchical nanoporous material [stage (iii), Fig. 2(c)]. It is apparent that the samples are monolithic, with dimensions in the millimeter regime. Optical and low-magnification scanning electron micrographs also reveal occasional macroscale cracks. The cracks were observed after the 2nd dealloying and could only be avoided for 0.76 V as dealloying potential, where crack-free samples are observed. As that latter condition results in the largest lower-level ligament size, we speculate that the cracks are

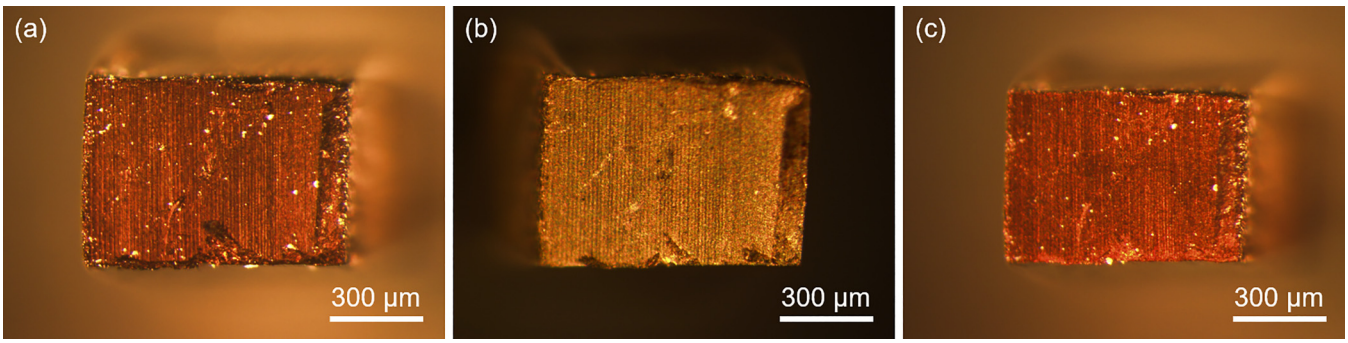

FIG. 2. Optical microscope images of samples in various stages of preparation. (a) Stage (i) sample after 1st dealloying to a composition of $Ag_{75}Au_{25}$; (b) stage (ii) sample after annealing at 400 °C; (c) stage (iii) sample after 2nd dealloying with a potential of 0.80 V.

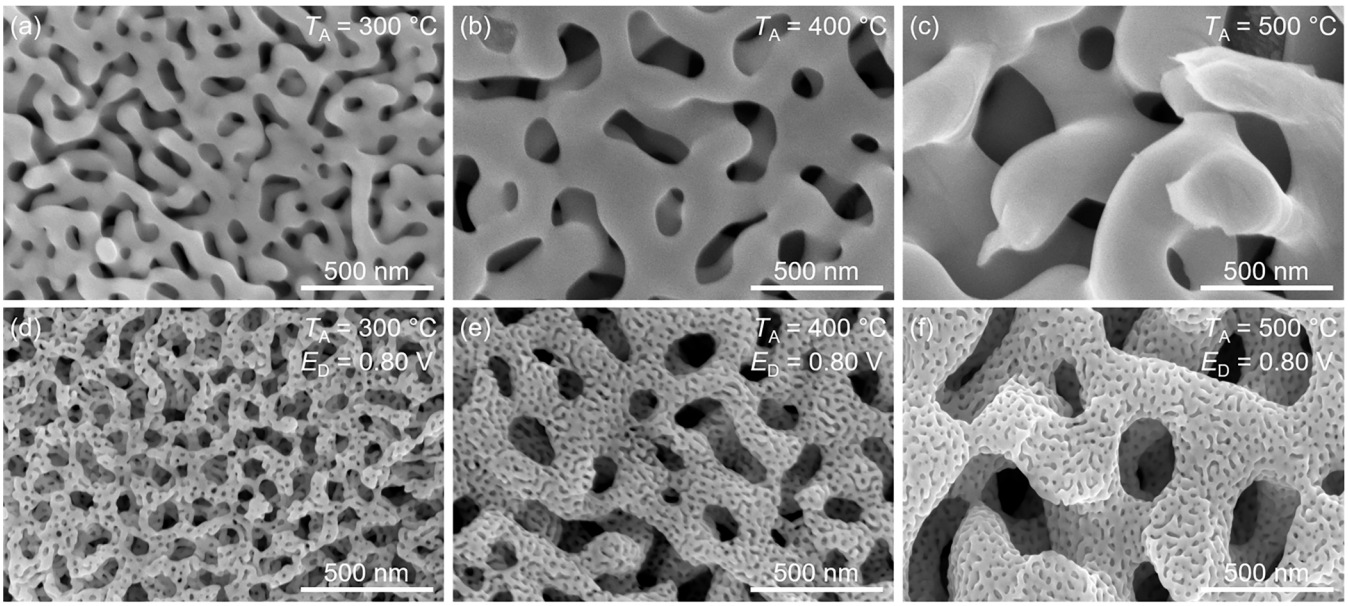

FIG. 3. Scanning electron micrographs showing impact of annealing treatment on microstructures of samples in stages (ii) and (iii). Top line: Stage (ii) nanoporous silver-gold. Bottom line: Stage (iii) hierarchical nanoporous gold prepared by dealloying at potential $E_D = 0.80$ V. Columns: Same annealing temperature, T_A. (a), (d): $T_A = 300\,^{\circ}$C; (b), (e): $T_A = 400\,^{\circ}$C; (c), (f): $T_A = 500\,^{\circ}$C. Note that L^U is maintained during the second dealloying. Note also nearly identical lower-hierarchy level ligament size.

not inherent to the dealloying procedure but that, instead, they originate in the large capillary pressures during drying, a well-known issue in the preparation of nanoporous materials [42].

For stage (i) samples, the solid fraction was determined as 0.41 ± 0.02. Solid fractions in stages (ii) and (iii) are listed in Table I.

Our experiments did not resolve the solid fractions on the individual hierarchy levels separately. Yet, an estimate of φ^U may be obtained based on results by Liu *et al.* [43]. For electrochemical dealloying of Au_xAg_{1-x} with $0.15 \leqslant x \leqslant 0.30$, that reference reports a linear relation between solid fraction and gold content suggesting $\varphi = 0.30$ at the value of our stage (ii) samples with $x = 0.25$. Taking $\varphi = 0.30$ as the solid fraction of the lower hierarchy level φ^L and using the values for the total solid fraction φ shown in Table I, the solid fraction of the upper level φ^U can be estimated as well. This suggests $\varphi^U = 0.50$, not too dissimilar from the solid fraction of the corresponding stage (ii) samples (see Table I).

B. Tuning the structure size at each hierarchy level

We have determined mean ligament diameters, L_{SEM}, by analysis of electron micrographs; see Methods. Stage (i) samples exhibit $L_{SEM} = 11 \pm 3$ nm ; see Fig. S2 in the Supplemental Material [32] for a scanning electron micrograph. Figure 3 illustrates the tuning of the ligament size at the upper hierarchy level in stage (ii) and (iii) samples, respectively, when T_A is varied. The identical E_D was used for all samples, and the lower-level ligament sizes are seen to emerge as closely similar. It is seen that the L^U_{SEM} value of stage (ii) is transferred to the hierarchical structure in stage (iii). L^U_{SEM} is tuned from 60 nm to 200 nm when T_A is varied from 300 °C to 500 °C.

Tuning the lower hierarchy level size by varying E_D while keeping T_A unchanged at 400 °C is illustrated in Fig. 4. An identical T_A here leads to a similar L^U_{SEM} irrespective of E_D. Regarding the lower level ligament size, dealloying at $E_D = 0.76$ V leads to $L^L_{SEM} = 29$ nm, whereas a higher E_D results in a smaller ligament size of $L^L_{SEM} \approx 20$ nm. This trend of a decreasing ligament size with increasing E_D can be explained by the adsorption of oxygen species on the surface at potentials higher than 0.78 V versus the Ag/AgCl pseudo-reference electrode. The oxygen species hinder the surface diffusion of gold, which results in less electrochemical coarsening, hence a smaller ligament size [44]. Similar observations have been reported for the dealloying of massive (nonporous) $Cu_{75}Au_{25}$ and $Ag_{75}Au_{25}$ in the same electrolyte [45,46]. Both studies specified the same potential for the transition from larger to smaller ligaments. In this context, it is worth noting that the residual silver content x^{res}_{Ag} listed in Table I is lowest for $E_D = 0.76$ V. This confirms most pronounced coarsening at the lowest E_D.

C. SAXS and USAXS signals

Figure 5 shows the SAXS and USAXS graphs of samples in various conditions. Panel (a) refers to stage (ii) NPSG samples, after 1st dealloying and annealing at different T_A. SEM images of these samples were presented in Figs. 3(a), 3(b), and 3(c) above. The well-known interference peak of dealloyed nanoporous gold is apparent in both the SAXS and the USAXS graphs. Increasing T_A is seen to shift the interference peak to lesser q_0, indicating larger structure size. The peak positions in SAXS and USAXS agree well, considering the resolution limits of the two approaches.

Figure 5(b) shows analogous scattering graphs for stage (iii) HNPG samples. These samples had experienced the

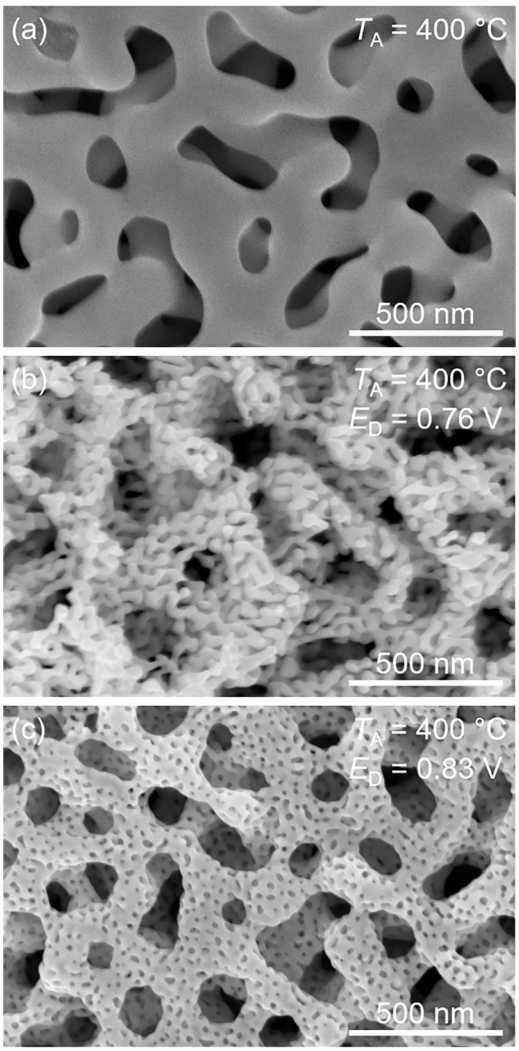

FIG. 4. Scanning electron micrographs showing impact of second dealloying potential E_D on microstructure in stage (iii). (a) Stage (ii) nanoporous silver-gold starting material, annealing temperature 400 °C, and upper hierarchy level ligament size $L^U = 130$ nm, as in Fig. 3(b). (b) $E_D = 0.76$ V. (c) $E_D = 0.83$ V.

identical set of annealing treatments as in panel (a), and they each experienced identical 2nd dealloying treatments, at $E_D = 0.80$ V. SEM images of these samples were presented in Figs. 3(e), 3(f), and 3(g) above. Their scattering graphs now exhibit two distinct interference peaks, which can be attributed to the lower and the upper hierarchy levels. The peaks originating in the upper level structure are located at q values quite similar to those of stage (ii) NPSG, indicating the retention of the upper-level structure when the lower level is generated by the second dealloying step. Furthermore, the positions of the peaks associated with the lower hierarchy level agree closely, supporting that identical dealloying potential during the second step results in identical structure size at the lower hierarchy level.

Figure 5(c) shows the results for HNPG samples prepared with the same $T_A = 400$ °C but with different E_D. SEM images of these samples were presented in Fig. 3(e) and Figs. 4(b) and 4(c) above. In the region of the upper-level interference peak, all SAXS scattering curves overlap. Furthermore, the USAXS peak positions agree. This supports the identical structure size at the upper hierarchy level. By contrast, the interference peak for the lower hierarchy level shifts to higher q_0 as E_D increases.

D. Characteristic length scales

We have determined ligament spacings from fits to the scattering graphs with combinations of Gaussians and baseline functions, as detailed in Sec. II D. Figure 6(a) exemplifies the high quality of the fits. In their limit of high q, we found the power law exponent of the baselines to be 4.0 ± 0.1, as expected for sharp interfaces in the Porod regime.

The characteristic spacings between ligaments on the upper and lower hierarchy levels, $\tilde{L}^U$ and $\tilde{L}^L$, were obtained from the peak centers of the Gaussians. Figures 6(b) and 6(c) show the $\tilde{L}$ versus the two synthesis variables T_A and E_D, respectively. For the $\tilde{L}^U$, the USAXS values vary between 97% and 102% of the SAXS ones. The excellent agreement validates the combination of SAXS and USAXS for the scale-bridging characterization of hierarchical porous structures with substantially different length scales on the individual hierarchy levels.

Figure 6(b) investigates the $\tilde{L}$ for the set of samples with identical E_D but different T_A. Combining SAXS and USAXS, $\tilde{L}^U$ in the range from 160 to 600 nm are resolved. The scattering experiments confirm the systematic increase of $\tilde{L}^U$ with the annealing temperature, while all samples have $\tilde{L}^L = 61 \pm 3$ nm, irrespective of T_A. Consistent with the preparation strategy, the $\tilde{L}^U$ of HNPG for $T_A = 300$ °C and 400 °C are close to the ligament spacings of the corresponding NPSG. A deviation for $T_A = 500$ °C is also apparent in the SEM images of Figs. 3(c) and 3(f). This observation may indicate structural heterogeneity after extensive coarsening.

Figure 6(c) refers to the set of samples with identical T_A but different E_D. The data confirm that $\tilde{L}^L$ can be tuned by the dealloying potential, while $\tilde{L}^U$ remains essentially constant. The set of samples quite consistently has $\tilde{L}^U = 303 \pm 18$ nm, while varying E_D from 0.76 V to 0.83 V decreases $\tilde{L}^L$ from 107 nm to 46 nm.

Figure 7(a) shows the ligament spacing values $\tilde{L}$ derived from small-angle scattering versus the SEM-derived ligament size values L_{SEM}. The figure combines data from each of the two hierarchy levels in a single graph, deliberately not discriminating between the levels. A straight-line fit through the origin provides

$$\tilde{L} \approx (2.7 \pm 0.1) L_{SEM}. \quad (7)$$

The narrow confidence limit and the linear correlation in the figure, extending over more than one order of magnitude in size, support that small-angle scattering provides for the independent characterization of sizes on each of the two hierarchy levels of HNPG, consistently with the evaluation of scanning electron micrographs.

The ligament spacing $\tilde{L}$ of the leveled-wave model has been related [14] to a mean ligament diameter, L_G, calculated by means of granulometry [47]. The results in [14] suggest values of 2.2, 2.0, and 1.8, respectively, for the ratio of $\tilde{L}/L_G$ in leveled-wave-like microstructures with $\varphi = 0.30$, 0.40, and

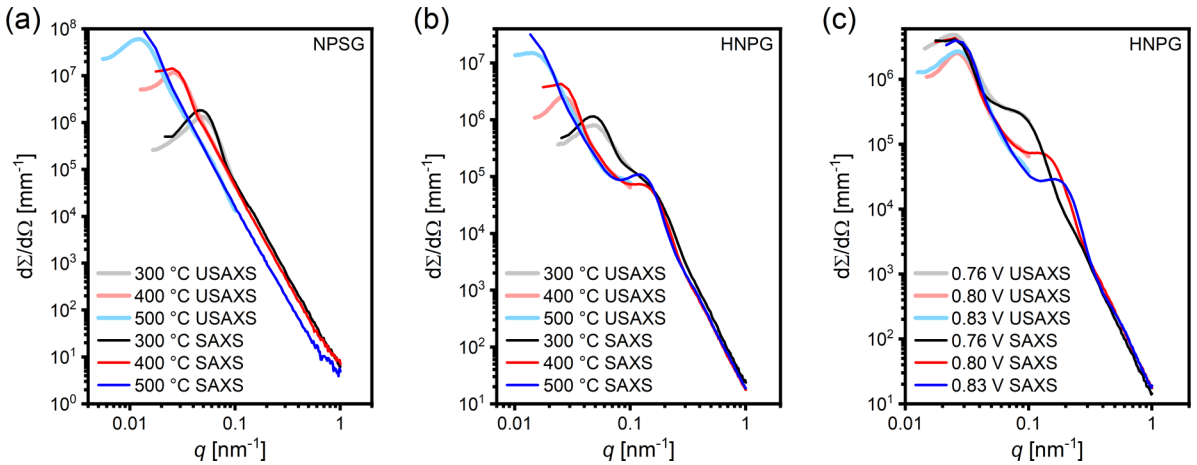

FIG. 5. Compilation of small-angle scattering (SAXS) and ultrasmall-angle scattering (USAXS) graphs of samples with different preparation conditions. The two synthesis variables, annealing temperature T_A and dealloying potential E_D, are indicated in legends. (a) Nanoporous silver-gold (NPSG) samples prepared with different T_A; (b) hierarchical nanoporous gold (HNPG) samples prepared with different T_A but identical $E_D = 0.80$ V; (c) HNPG samples prepared with same $T_A = 400\,^{\circ}$C but different E_D.

0.50. That range of φ covers the present samples, which have roughly $\varphi^L = 0.3$ at the lower and $\varphi^U = 0.5$ at the upper hierarchy level. So far, the relation between $\tilde{L}$ and L_{SEM} had remained unexplored. Our Eq. (7) indicates the value of the conversion factor. Remarkably, a single value of the conversion factor describes the structure at both levels of our hierarchical material.

The quite large difference between $\tilde{L}$ and L_{SEM} can be understood since the distance between neighboring ligaments is expected roughly twice the ligament diameter, when volume fractions of ligaments and pores are not too dissimilar. Furthermore, L_{SEM} measures for the ligaments' dimensions at their narrowest diameter and this contributes further to increasing the difference to $\tilde{L}$.

E. Specific surface area

NPG-based functional materials, for instance for catalysis or actuation, rely on high values of their specific surface area α. We evaluated α from the scattering data by means of Eq. (4), starting out with assessing the analysis of the invariant, Q. Comparing values of Q based on integrating the scattering intensity, Eq. (2) for Q_S, and on data for the net solid fraction, Eq. (3) for Q_φ, we found the ratio Q_S/Q_φ as 0.82 ± 0.18. This qualifies the reduction of the scattering data to differential scattering cross section as sensibly correct. We note that errors in the normalization of the scattering data to absolute units cancel out in Eq. (4) for α, since they affect Q_S and the high-q limit of $d\Sigma/d\Omega$ in the same way.

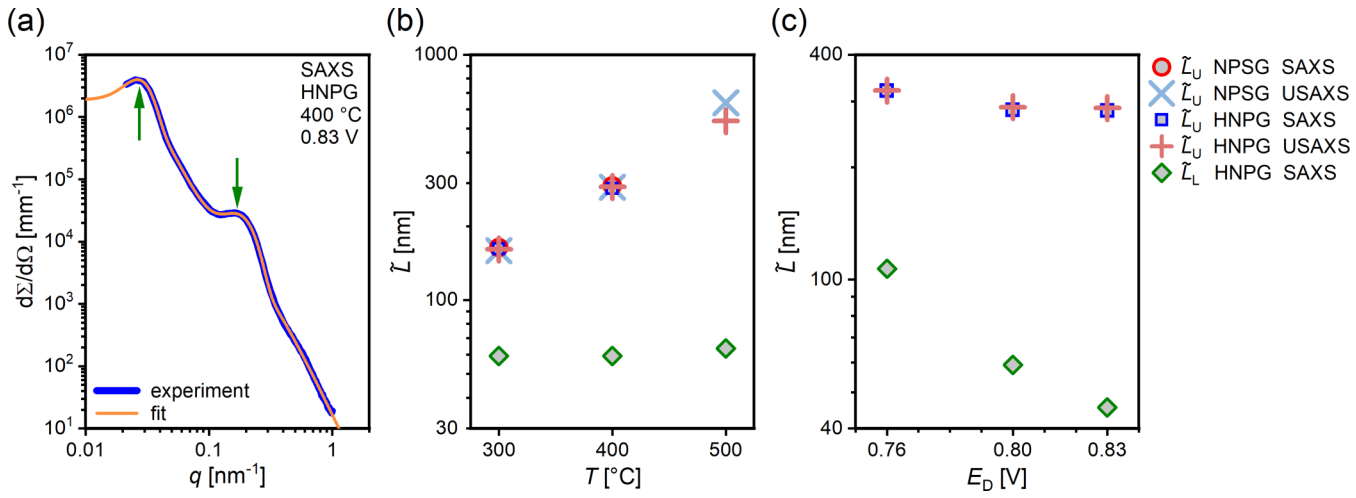

FIG. 6. Evaluation of ligament spacings, $\tilde{L}$, by analysis of interference peak positions. (a) Exemplary experimental scattering curve (bold blue line) with fit (orange line) superimposed. The peak position according to the fit is marked by an arrow. (b) Results for samples from Figs. 5(a) and 5(b) for stage (ii) nanoporous silver-gold (NPSG) and stage (iii) hierarchical nanoporous gold (HNPG) samples. Different annealing temperature T_A and identical dealloying potential. Ligament spacings at upper ($\tilde{L}^U$) and lower ($\tilde{L}^L$) hierarchy levels determined from small-angle scattering (SAXS) and ultrasmall-angle scattering (USAXS), as indicated in legend. Note tuning of upper hierarchy level ligament size at constant size on lower level. (c) As in (b), but for samples from Fig. 5(c), HNPG samples with identical T_A, and different dealloying potential E_D. Note tuning of lower hierarchy level ligament size at constant size on upper level.

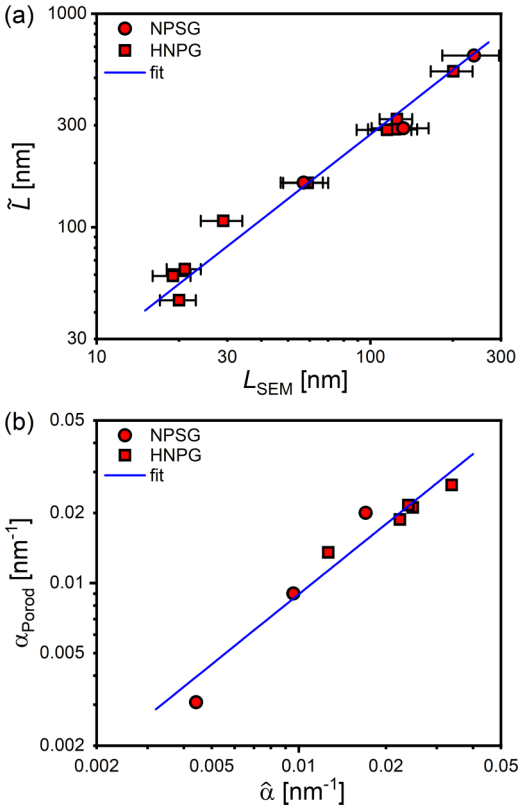

FIG. 7. Comparing different approaches to metrics for the microstructure of nanoporous silver-gold (NPSG) and hierarchical nanoporous gold (HNPG). (a) Ligament spacing $\tilde{L}$ derived from the scattering data along with Eq. (1), plotted against ligament size L_{SEM} determined by analysis of scanning electron micrographs. Error bars indicate the standard deviation in L_{SEM}. If both a SAXS and a USAXS measurement exist, the ligament spacing value is the average of both values. Line: Slope 1 (linear correlation) straight line of best fit, with a slope of 2.7. (b) Specific surface area α_{Porod} derived from the analysis of the Porod region [Eq. (4)] in small-angle scattering versus the specific surface area, $\hat{\alpha}$, of the leveled-wave model, using data for ligament spacing and solid fraction in Eq. (5) or (6). Line: Slope 1 (linear correlation) straight line of best fit, with a slope of 0.90.

Figure 7(b) shows a comparison between the specific surface area values, α_{Porod}, determined by analysis of the Porod region using Eq. (4) and the specific surface area, $\hat{\alpha}$, determined by analysis of the SAXS and USAXS peak positions with Eqs. (5) and (6). If for a peak position both a SAXS and a USAXS measurement value exist, then the average of both values was used. A straight line of best fit provides $\alpha_{Porod} = (0.90 \pm 0.05)\hat{\alpha}$. This finding qualifies small-angle scattering as an interesting approach to measuring α. We also note the good agreement between the model-independent measure for α, based on the Porod prefactor, and the value estimated based on the leveled-wave geometry. The agreement adds support to the leveled-wave model as a valid approximation of the microstructure of nanoporous gold.

Our discussion of the microstructure of HNPG treats the volume-specific surface area α as a variable with a natural link to the geometry. The mass-specific surface area, α_m, by contrast involves the bulk mass density ρ_m as an extrinsic parameter, not related to the geometry or to the scattering experiment. That being said, conversion between the two metrics is straightforward for our materials, since ρ_m can be inferred from their known composition (Table I). Using $\alpha_m = \alpha/(\varphi\rho_m)$, it is found that the intervals in α of Fig. 7(b) imply $\alpha_m = 0.6$–4.0 m^2 g^{-1} for NPSG and 5.0–10.3 m^2 g^{-1} for HNPG.

Several approaches are available for the relation of the ligament diameter to the specific surface area [45,48–50]. Arguably, the one based on the leveled-wave structure [14] exploits the most detailed microstructural model for NPG. Indeed, we find good agreement between our values and the leveled-wave result. Here again, it is remarkable that this agreement continues to hold when one goes from single-scale NPG to the hierarchical material.

IV. CONCLUSIONS

Our study of hierarchical nanoporous gold made by two-step dealloying confirms that the characteristic microstructural length scales on each of the material's two hierarchy levels can be independently controlled through the synthesis parameters. We find that the combined small-angle and ultrasmall-angle scattering approach, working on focused-ion-beam-cut specimens, provides access to the key microstructural parameters, the characteristic length scales, and the specific surface area.

The interference peaks of the scattering experiments afford measuring a characteristic ligament spacing. We have found this to correlate well with mean ligament diameters determined by analysis of scanning electron micrographs; the ratio between both metrics for size is 2.7 ± 0.1. This finding may afford comparability between studies reporting either of the two distinct metrics.

Overall, the results of this work promote the production of hierarchical nanoporous materials for the future design of lightweight materials. Furthermore, the characterization method described in this text can be applied to nanoporous materials in general to describe and compare their structural size.

ACKNOWLEDGMENT

This work was supported by the Deutsche Forschungsgemeinschaft (DFG) within the Collaborative Research Initiative CRC 986 "Tailor-Made Multi-Scale Materials Systems" (Project No. 192346071).

[1] Y. Ding and J. Erlebacher, Nanoporous metals with controlled multimodal pore size distribution, J. Am. Chem. Soc. **125**, 7772 (2003).

[2] Z. Zhang, Y. Wang, Z. Qi, J. Lin, and X. Bian, Nanoporous gold ribbons with bimodal channel size distributions by chemical dealloying of Al-Au alloys, J. Phys. Chem. C **113**, 1308 (2009).

[3] Z. Qi and J. Weissmüller, Hierarchical nested-network nanostructure by dealloying, ACS Nano **7**, 5948 (2013).

[4] Z. Qi, U. Vainio, A. Kornowski, M. Ritter, H. Weller, H. Jin, and J. Weissmüller, Porous gold with a nested-network architecture and ultrafine structure, Adv. Funct. Mater. **25**, 2530 (2015).

[5] T. Fujita, Y. Kanoko, Y. Ito, L. Chen, A. Hirata, H. Kashani, O. Iwatsu, and M. Chen, Nanoporous metal papers for scalable hierarchical electrode, Adv. Sci. **2**, 1500086 (2015).

[6] X. Guo, J. Han, P. Liu, L. Chen, Y. Ito, Z. Jian, T. Jin, A. Hirata, F. Li, T. Fujita, N. Asao, H. Zhou, and M. Chen, Hierarchical nanoporosity enhanced reversible capacity of bicontinuous nanoporous metal based Li-O_2 battery, Sci. Rep. **6**, 33466 (2016).

[7] T. Fujita, Hierarchical nanoporous metals as a path toward the ultimate three-dimensional functionality, Sci. Technol. Adv. Mater. **18**, 724 (2017).

[8] S. Shi, Y. Li, B.-N. Ngo-Dinh, J. Markmann, and J. Weissmüller, Scaling behavior of stiffness and strength of hierarchical network nanomaterials, Science **371**, 1026 (2021).

[9] Y. Shi, Y. Zhang, B. Yu, K. Yin, J. Qin, and Z. Zhang, Porous gold with three-level structural hierarchy, iScience **25**, 105113 (2022).

[10] T. Yu, X. Zhou, Y. Chen, J. Chen, S. Yuan, Z. Zhang, L. Qian, and S. Li, Robust catalysis of hierarchically nanoporous gold for CO_2 electrochemical reduction, Electrochim. Acta **437**, 141537 (2023).

[11] F. Tan, B. Yu, Y. Wang, Q. Bai, and Z. Zhang, Hierarchically structured nanoporous palladium with ordered/disordered channels for ultrahigh and fast strain, Nano Lett. **23**, 505 (2023).

[12] T. Juarez, J. Biener, J. Weissmüller, and A. M. Hodge, Nanoporous metals with structural hierarchy: A review, Adv. Eng. Mater. **19**, 1700389 (2017).

[13] C. Wang and Q. Chen, Reduction-induced decomposition: Spontaneous formation of monolithic nanoporous metals of tunable structural hierarchy and porosity, Chem. Mater. **30**, 3894 (2018).

[14] C. Soyarslan, S. Bargmann, M. Pradas, and J. Weissmüller, 3D stochastic bicontinuous microstructures: Generation, topology and elasticity, Acta Mater. **149**, 326 (2018).

[15] C. Zhu, Z. Qi, V. A. Beck, M. Luneau, J. Lattimer, W. Chen, M. A. Worsley, J. Ye, E. B. Duoss, C. M. Spadaccini, C. M. Friend, and J. Biener, Toward digitally controlled catalyst architectures: Hierarchical nanoporous gold via 3D printing, Sci. Adv. **4**, eaas9459 (2018).

[16] S. Mooraj, S. S. Welborn, S. Jiang, S. Peng, J. Fu, S. Baker, E. B. Duoss, C. Zhu, E. Detsi, and W. Chen, Three-dimensional hierarchical nanoporous copper via direct ink writing and dealloying, Scr. Mater. **177**, 146 (2020).

[17] P. Sondhi and K. J. Stine, Methods to generate structurally hierarchical architectures in nanoporous coinage metals, Coatings **11**, 1440 (2021).

[18] I. McCue, J. Stuckner, M. Murayama, and M. J. Demkowicz, Gaining new insights into nanoporous gold by mining and analysis of published images, Sci. Rep. **8**, 6761 (2018).

[19] R. Newman, S. Corcoran, J. Erlebacher, M. Aziz, and K. Sieradzki, Alloy corrosion, MRS Bull. **24**, 24 (1999).

[20] E. J. Schofield, B. Ingham, A. Turnbull, M. F. Toney, and M. P. Ryan, Strain development in nanoporous metallic foils formed by dealloying, Appl. Phys. Lett. **92**, 043118 (2008).

[21] C. J. Dotzler, B. Ingham, B. N. Illy, K. Wallwork, M. P. Ryan, and M. F. Toney, *In situ* observation of strain development and porosity evolution in nanoporous gold foils, Adv. Funct. Mater. **21**, 3938 (2011).

[22] B. Lin, L. Kong, P. D. Hodgson, S. Mudie, A. Hawley, and L. F. Dumée, Controlled porosity and pore size of nano-porous gold by thermally assisted chemical dealloying—a SAXS study, RSC Adv. **7**, 10821 (2017).

[23] B. Lin, M. Döbeli, S. Mudie, A. Hawley, P. Hodgson, L. Kong, R. Spolenak, and L. F. Dumée, An *in-situ* small angle x ray scattering analysis of nanopore formation during thermally induced chemical dealloying of brass thin foils, Sci. Rep. **8**, 15419 (2018).

[24] S. S. Welborn and E. Detsi, Small-angle x-ray scattering of nanoporous materials, Nanoscale Horiz. **5**, 12 (2020).

[25] S. S. Welborn, S. van der Meer, J. S. Corsi, J. T. M. de Hosson, and E. Detsi, Using x-ray scattering to elucidate the microstructural instability of 3D bicontinuous nanoporous metal scaffolds for use in an aperiodic 3D tricontinuous conductor–insulator–conductor nanocapacitor, ACS Appl. Mater. Interfaces **13**, 11721 (2021).

[26] J. S. Corsi, S. S. Welborn, E. A. Stach, and E. Detsi, Insights into the degradation mechanism of nanoporous alloy-type Li-ion battery anodes, ACS Energy Lett. **6**, 1749 (2021).

[27] A. K. Ng, S. S. Welborn, and E. Detsi, Time-dependent power law function for the post-dealloying chemical coarsening of nanoporous gold derived using small-angle x-ray scattering, Scr. Mater. **206**, 114215 (2022).

[28] M. Gößler, E. Hengge, M. Bogar, M. Albu, D. Knez, H. Amenitsch, and R. Würschum, *In situ* study of nanoporosity evolution during dealloying AgAu and CoPd by grazing-incidence small-angle x-ray scattering, J. Phys. Chem. C **126**, 4037 (2022).

[29] J. W. Cahn, Phase separation by spinodal decomposition in isotropic systems, J. Chem. Phys. **42**, 93 (1965).

[30] B. Zandersons, L. Lührs, Y. Li, and J. Weissmüller, On factors defining the mechanical behavior of nanoporous gold, Acta Mater. **215**, 116979 (2021).

[31] W. Rasband, ImageJ, National Institute of Health, Bethesda, Maryland, USA, https://imagej.net/ij/download.html.

[32] See Supplemental Material at http://link.aps.org/supplemental/10.1103/PhysRevMaterials.7.116001 for an illustration of the ligament diameter determination and an additional SEM micrograph of a stage (i) sample after 1st dealloying.

[33] M. Sztucki, J. Gorini, J.-P. Vassalli, L. Goirand, P. van Vaerenbergh, and T. Narayanan, Optimization of a Bonse-Hart instrument by suppressing surface parasitic scattering, J. Synchrotron Radiat. **15**, 341 (2008).

[34] Xenocs, XSACT: X-ray Scattering Analysis and Calculation Tool, https://www.xenocs.com/saxs-products/xsact-software, SAXS and WAXS data analysis software – Version 2.4.

[35] J. Lake, An iterative method of slit-correcting small angle x-ray data, Acta Crystallogr. **23**, 191 (1967).

[36] T. Fujita and M. W. Chen, Characteristic length scale of bicontinuous nanoporous structure by fast Fourier transform, Jpn. J. Appl. Phys. **47**, 1161 (2008).

[37] C. Mahr, P. Kundu, A. Lackmann, D. Zanaga, K. Thiel, M. Schowalter, M. Schwan, S. Bals, A. Wittstock, and A.

Rosenauer, Quantitative determination of residual silver distribution in nanoporous gold and its influence on structure and catalytic performance, J. Catal. **352**, 52 (2017).

[38] A. Michels and J. Weissmüller, Magnetic-field-dependent small-angle neutron scattering on random anisotropy ferromagnets, Rep. Prog. Phys. **71**, 066501 (2008).

[39] P. Debye Jr., H. Anderson Jr., and H. Brumberger, Scattering by an inhomogeneous solid. II. The correlation function and its application, J. Appl. Phys. **28**, 679 (1957).

[40] G. Porod, General theory, in *Small Angle X-Ray Scattering*, edited by O. Glatter and O. Kratky (Academic Press, New York, 1982), pp. 17–51.

[41] D. S. Sivia, *Elementary Scattering Theory: For X-ray and Neutron Users* (Oxford University Press, New York, 2011).

[42] D. Bellet and L. Canham, Controlled drying: The key to better quality porous semiconductors, Adv. Mater. **10**, 487 (1998).

[43] F. Liu, X.-L. Ye, and H.-J. Jin, Anomalous low strain induced by surface charge in nanoporous gold with low relative density, Phys. Chem. Chem. Phys. **19**, 19217 (2017).

[44] X.-L. Ye and H.-J. Jin, Electrochemical control of creep in nanoporous gold, Appl. Phys. Lett. **103**, 201912 (2013).

[45] Y. Zhong, J. Markmann, H.-J. Jin, Y. Ivanisenko, L. Kurmanaeva, and J. Weissmüller, Crack mitigation during dealloying of $Au_{25}Cu_{75}$, Adv. Eng. Mater. **16**, 389 (2014).

[46] X.-L. Ye, N. Lu, X.-J. Li, K. Du, J. Tan, and H.-J. Jin, Primary and secondary dealloying of Au(Pt)-Ag: Structural and compositional evolutions, and volume shrinkage, J. Electrochem. Soc. **161**, C517 (2014).

[47] T. Hildebrand and P. Rüegsegger, A new method for the model-independent assessment of thickness in three-dimensional images, J. Microsc. **185**, 67 (1997).

[48] E. Detsi, E. De Jong, A. Zinchenko, Z. Vuković, I. Vuković, S. Punzhin, K. Loos, G. ten Brinke, H. A. De Raedt, P. R. Onck, and J. T. M. De Hosson, On the specific surface area of nanoporous materials, Acta Mater. **59**, 7488 (2011).

[49] B.-N. D. Ngô, A. Stukowski, N. Mameka, J. Markmann, K. Albe, and J. Weissmüller, Anomalous compliance and early yielding of nanoporous gold, Acta Mater. **93**, 144 (2015).

[50] H. Jeon, N.-R. Kang, E.-J. Gwak, J.-i. Jang, H. N. Han, J. Y. Hwang, S. Lee, and J.-Y. Kim, Self-similarity in the structure of coarsened nanoporous gold, Scr. Mater. **137**, 46 (2017).